Which Spring is the Best? Comparison of Methods for Virtual Stenting

Katerina Spranger* and Yiannis Ventikos

***Abstract*—This paper presents a methodology for modeling the deployment of implantable devices used in minimally invasive vascular interventions. Motivated by the clinical need to perform preinterventional rehearsals of a stent deployment, we have developed methods enabling virtual device placement inside arteries, under the constraint of real-time application. This requirement of rapid execution narrowed down the search for a suitable method to the concept of a *dynamic mesh*. Inspired by the idea of a mesh of springs, we have found a novel way to apply it to stent modeling. The experiments conducted in this paper investigate properties of the stent models based on three different spring types: lineal, semi-torsional, and torsional springs. Furthermore, this paper compares the results of various deployment scenarios for two different classes of devices: a stent graft and a flow diverter. The presented results can be of a high-potential clinical value, enabling the predictive evaluation of the outcome of a stent deployment treatment.**

***Index Terms*—Flow diverter, modeling, stent, virtual stenting.**

I. Introduction

MINIMALLY invasive vascular interventions have become a popular alternative to conventional open surgery in the treatment of many vascular disorders, such as aneurysms, aortic dissections, and atherosclerotic stenoses [1], [2]. Minimally invasive endovascular repair is performed through small incisions, usually made in the femoral artery, from where a prosthesis or *stent*[1] is pushed to a target location, under fluoroscopic guidance and using a catheter, where it is subsequently deployed inside the diseased vessel. Compared to open surgery, endovascular repair leads to better treatment outcomes, including less complications, less blood loss, shorter surgery times, and hospital stays, etc., mainly attributed to its minimally invasive nature [3]–[5].

However, the high initial success rates of endovascular repairs have been shadowed by reported complications, for example, stroke, thromboembolism, and luminal restenosis, that cause reinterventions and, in the worst case, morbidity and mortality [6], [7]. Similarly, endovascular repair of cerebral aneurysms can sometimes provoke an occasional hemorrhagic event that follows an initially successful treatment. In approximately 1% of cases, the subsequent rupture of the treated cerebral aneurysms is reported between a few days and 3–4 months after the treatment [5]. With respect to stroke, the new rate of 6% has been recently established by the "Pipeline Embolization Device in the Intracranial Treatment of Aneurysms (PITA)" trial [8], which is unacceptably high and could threaten the general use of flow diverters (FDs) in the future.

It is known that a number of factors play an important role in the outcome of the stent deployment procedure; the key players being the target vessel's geometry and hemodynamics, design and the placement position of the implant, incidence of an arterial injury during the intervention, etc. [9]. For example, it has been reported that neointimal hyperplasia can initiate from arterial injury during the procedure and cause significant stenosis [10]. In general, vessel remodeling can play an important part in these processes [11]. Additionally, several studies have suggested that injuries can also occur after the intervention, caused by the nonuniform expansion of the device or its excessive axial contraction [9]. On the other hand, incomplete contact between the stent-filaments and the arterial wall can increase the risk of intimal hyperplasia [12], and stent underexpansion can lead to in-stent thrombosis [13].

The dangerous complications caused by arterial injury and inadequate device apposition could be mitigated by better choice of the stent design [14] and by the appropriate positioning of the implant inside the vessel [15], [16]. However, there is currently no possibility for a clinician to predict the resulting position and the expanded shape of the device for a given patient before the intervention in a clinical setting. Moreover, knowing the accurate configuration of the device, its attachment to the vessel wall, especially the level of covering of the aneurysmal neck or dissection's entries, would enable the subsequent study of the postinterventional alterations in the hemodynamic environment of the vessel. Subsequent hemodynamic analysis [17] can provide early indications for such complications as stent graft (SG) migration, endoleakage [18], endotension [19], thrombus formation, etc.

Although there have been numerous attempts to study the process of stent deployment computationally, they all feature considerable limitations when judged upon their suitability for clinical practice. The approaches reported in the literature can be roughly divided into finite-element analysis (FEA) methods and fast virtual stenting techniques. With respect to FEA methods,

Manuscript received October 10, 2013; revised January 20, 2014; accepted March 3, 2014. Date of publication March 14, 2014; date of current version June 14, 2014. The work of Katerina Spranger was supported by the Centenary Year Graduate Scholarship, Dept. of Engineering Science, University of Oxford. The work of Yiannis Ventikos was supported by the Wellcome Trust/EPSRC, Centre of Excellence in Personalized Healthcare, under Grant WT 088877/Z/09/Z. *Asterisk indicates corresponding author.*

*K. Spranger is with the Department of Engineering Science, University of Oxford, Oxford, OX1 2JD, U.K. (e-mail: katerina.spranger@eng.ox.ac.uk).

Y. Ventikos is with the Department of Mechanical Engineering, University College London, London, WC1E 6BT, U.K. (e-mail: y.ventikos@ucl.ac.uk).

Color versions of one or more of the figures in this paper are available online at http://ieeexplore.ieee.org.

Digital Object Identifier 10.1109/TBME.2014.2311856

[1]"Stent" will be used to denote stent grafts and flow diverters, for brevity.

there has been a lot of work carried out to analyze the mechanical behavior of stents as well as simulating their implantation. The themes range from studies on the expansion mechanisms [20], to deployment of the device within patient-specific anatomies [21], interactions with the vessel wall [22], and implications on the local hemodynamics [23]. Although highly accurate, these FEA models were not aimed for usage in clinical practice on a day-to-day basis, where the speed of computations becomes a crucial factor.

In contrast to FEA studies, the second category of the fast virtual methods feature severe simplifications in crucial aspects of the process. Literature survey has revealed only three approaches to stent deployment simulations that aim at evaluating different stent and release scenarios on a patient-specific, clinically relevant basis. In the methodology proposed in [24], the model is initiated by placing a cylinder along the centerline of a vessel and then deforming it to follow the centerline curvature. Such mapping of the stent geometry as a texture over a cylinder may have implications on the accuracy of stent configurations, especially in regions of high curvature of the vessel. Another study, [25], models a stent as a deforming cylinder, which is first positioned inside the vessel and thereafter serves as a basis for the reconstruction of the struts' configuration. Similar to the previous approach, this method merely deforms a generic cylindrical structure and does not sufficiently account for the geometrical properties and the design of the device, and its interaction with the vessel. The third method, [26], explicitly models the stent design by capturing the design elements as soft constrains; however, complex vessel geometries challenge the accuracy of this computational method.

Motivated by clinical need and lack of suitable methods, this study aims at developing a methodology for modeling the virtual deployment of implantable devices inside patients' vessels that features fast computational times and can be used in the clinical practice. Ultimately, such a capability can play a transformative role in aiding clinical decision making in intravascular interventions on a personalized basis and also give rise to overall improvements in the implant design and deployment procedure. We will target interventions performed under radiological guidance both in the abdominal and intracranial areas. Hence, the methodology should be general enough to be able to include a broad range of devices, such as SGs and FDs. With this in mind, we have narrowed down the investigated computational techniques to those that are both sufficiently generic and computationally inexpensive.

Our attention was drawn to the class of methods called *deformable models* that are widely used in many engineering applications [27]. One version particularly suitable for medical applications is called the *elastic analogy*, where a deforming body is viewed as an elastic structure, whose deformation is then guided by elastic forces. The elastic analogy in its discrete version is sometimes referred to as the *spring analogy*; here, mesh edges are treated as artificial springs generating springs' forces, and deformations are governed by the condition of static equilibrium [28]. In the literature, these approaches are often subsumed under the category of the *dynamic mesh* algorithms and are of a great relevance due to their simplicity of implementation and relatively low computational complexity.

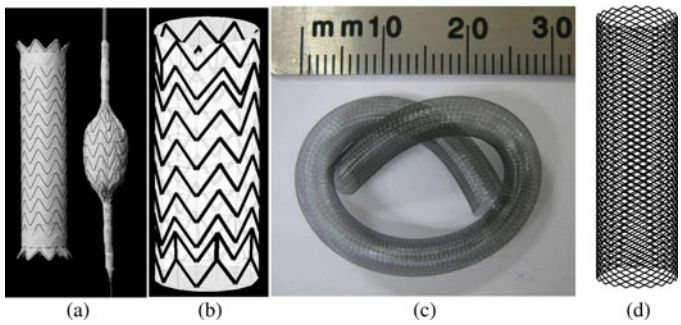

Fig. 1. Reconstruction of stents. (a) Gore TAG thoracic endoprosthesis in the load-free and partially expanded configuration (image from [29]). (b) Computational representation of the SG (4 cm×10 cm). (c) PED from ev3, Irvine, CA, USA (image from [30]). (d) Reconstructed 3-D struts mesh representing the PED (3 mm×14 mm).

In this paper, we investigate the suitability of the dynamic mesh approaches to the stent deployment problem and report the results of comparison of three different springs analogy methods. We start by describing the overall methodology (see Section II) involved in the virtual stent deployment. This section includes the preprocessing of the devices and vessels data as well as the modeling of the expansion process. The three springs analogy methods investigated are 1) the lineal, 2) semitorsional, and 3) torsional springs, in order of increasing complexity. Their results are compared for two different types of devices: a SG and a FD, representing the most widely used classes of endovascular implants (see Section III). The comparison is performed on different deployment scenarios: 1) in the case of free expansion, 2) in idealized straight vessels, 3) in idealized bent vessels, and 4) in real patient vasculature. The primary goal of the comparisons is to determine whether the use of the more computationally intensive version is eventually justified by the increasing realism of the results. We conclude by discussing the results and limitations of this study and outline planned future directions (see Section IV).

II. Methodology

A. Preprocessing of Endovascular Stents

This section outlines the initial steps required to create the model of the stent and prepare it for the expansion process.

1) Geometry Reconstruction: SGs are usually comprised of an external self-expanding nitinol wire structure (struts) that is attached to the surface of the graft [see Fig. 1(a)]. We reconstructed the design of the struts from an X-ray computed tomography scan of the device with the spatial resolution of around 150 μm. The strut wires are approximated by their centerlines, i.e., they are initially modeled without an explicit thickness to enable fast deployment (the thickness is restored for the subsequent CFD analysis). Afterward, the struts' centerline representation is supplemented with a background mesh that emulates the device's sheath and prevents an excessive expansion and

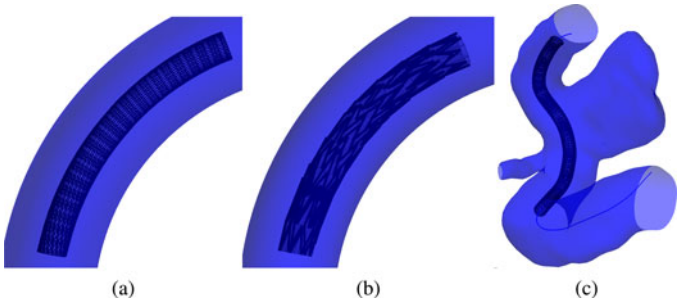

Fig. 2. Initial positioning of the crimped stent along the centerline of the vessel. (a) 30%-crimped generic stent. (b) 30%-crimped SG. (c) 20%-crimped FD in a patient-specific geometry.

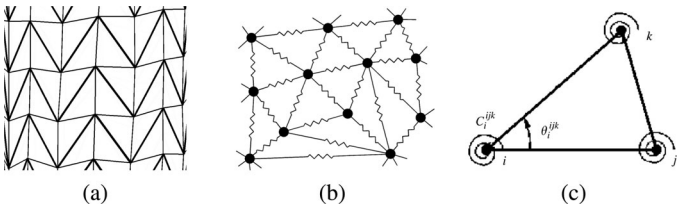

Fig. 3. (a) SG mesh: thick lines show struts and thin lines—the background mesh. (b) Schematic representation of the lineal spring analogy: each edge of the mesh is viewed as a lineal spring. (c) In the semitorsional spring analogy, artificial torsional springs are added to each node of a mesh [34].

distortion of the stent during deployment. The merging of the two meshes (struts and background) can be achieved in two ways: using an isotropic triangulation in which the stent geometry has been given a "best-fit" representation within the background mesh or creating an anisotropic mesh using triangulation constraints, i.e., requiring mesh elements to incorporate the stent struts (see Figs. 1(b) and 3(a) for a zoomed element).

Due to the high porosity, high pore density, and regular struts architecture, the easiest way to model a typical FD (or devices of a similar design) is to use the CAD software to replicate its design. After a 2-D representation has been obtained with CAD, the sheet can then be wrapped around a cylinder to get a 3-D structure. Fig. 1(c) and (d) shows an example geometry for the commercially available Pipeline Embolization Device (PED, ev3, Irvine, CA, USA). Since FDs have no sheath, there is no need for an additional background mesh.

2) Local Coordinates: For later manipulations of the stent geometry, it is convenient to establish a local coordinate system for the device in order to decouple the mechanical component of computations from the stent positioning in the global coordinate system. The local coordinates can be set along the principal axes of the stent that can be obtained by a principal component analysis performed on the stent vertices. After the analysis, the first component gives the centerline of the stent, whereas the second and third components lie in its circumferential plane.

3) Crimped Configuration: During the minimally invasive stent deployment in the clinical setting, the vascular prosthesis is first crimped and placed into a delivery system. Upon release in a target vessel location, it "springs" back to a load-free configuration under the elastic forces of the material. Currently, most self-expanding devices are made of nitinol (nickel–titanium alloy), which is a superelastic material, that features an elastic response to small deformations of up to 10%, whereas larger strains can be achieved superelastically due to its shape-memory effect [31].

Thus, we have to start the deployment simulation with the crimping of the device. In order to compute the crimped configuration, we prescribe the displacements to the stent nodes with respect to the load-free configuration. Sometimes the crimping leads to a foreshortening effect, whereby the stent is becoming shorter when deployed, which is observed in real stents, especially, in the case of FDs.

4) Initial positioning: After the stent has been crimped, the next step in a minimally invasive procedure is the positioning of the catheter in a desired location inside the vessel with the help of a guidewire. Both the guidewire and the catheter are flexible enough to be able to follow the curvature of the vessel they are being pushed through. Once the target destination is reached, such as the neck of an aneurysm or desirable entry in the case of an aortic dissection, the catheter is pulled out to release the stent which starts expanding under the elastic forces of nitinol it is made of (for self-expanding devices).

In order to simulate the initial placement of the device before its release out of the catheter, we deform the crimped device in a way to let it follow the curvature of the vessel's centerline. First, all vertices of the stent are divided into layers depending on their longitudinal position in the stent's local coordinates. Afterward, we deform each layer of the stent according to the deviation of the corresponding vessel's centerline point from the straight line—centerline of the stent. The prescribed displacements for both the crimping and bending procedure give rise to restoring forces acting in the stent structure. The results of these preparatory steps can be seen in Fig. 2, which shows the placement of three different crimped stents along the centerline of the vessel.

B. Modeling Expansion

In this section, we explore and compare different fast computational methods in order to determine the most suitable approach for modeling the process of stent expansion. First, we briefly describe the overall theoretical framework of the dynamic mesh approaches and then zoom into the details of the three exemplar methods and show how to apply them to the stent expansion problem. The three versions employed are 1) the lineal spring analogy, 2) the semitorsional spring analogy, and 3) the torsional spring analogy. All three versions are approximative methods; however, they feature increasing complexity and precision of the iterative equations. Our ultimate goal will be to investigate their suitability for modeling the stent expansion process and finding out whether the more computationally intensive version is justified by a concomitant increase in precision. In assessing the precision, we are mostly interested in the final configuration of the deployed device (and not in the transient states) as this constitutes the clinically relevant component, especially with respect to the possible subsequent CFD analysis.

1) Theoretical Framework: The methods we have focused on fall under the category of *dynamic meshes*, which were originally proposed as a means of dealing with the *moving boundary*

problems that involve the deformation of the computational domain during simulation. In our approach, we will be modeling the stent structure as a dynamic mesh.

A dynamic mesh is often viewed as a continuous or discrete pseudostructural system with fictitious mass, damping, and stiffness properties [32]. Then, the movement of such a mechanical system obeys the semidiscrete equations of dynamic equilibrium

$$\mathbf{M}\ddot{\mathbf{q}} + \mathbf{D}\dot{\mathbf{q}} + \mathbf{K}\mathbf{q} = 0; \tag{1}$$

where $\mathbf{M}, \mathbf{D}$, and $\mathbf{K}$ are the system's fictitious mass, damping, and stiffness matrices, respectively; $\dot{\mathbf{q}}$ indicates a time-derivative of the displacement vector $\mathbf{q}$ which is defined by

$$\mathbf{q}(t) = \boldsymbol{\xi}(t) - \boldsymbol{\xi}(0), \tag{2}$$

with t representing time and $\boldsymbol{\xi}$ standing for the coordinates vector of mesh vertices [32].

The displacement boundary condition is often accompanying the dynamic equilibrium equation

$$\mathbf{q}(t) = \bar{\mathbf{q}}(t) \tag{3}$$

on $\boldsymbol{\Gamma}_m$, with $\bar{\mathbf{q}}(t)$ representing the known displacements of the moving boundary $\boldsymbol{\Gamma}_m$. Usually, the boundary nodes of $\boldsymbol{\Gamma}_m$ remain at the same relative positions after the movement, whereas the new positions of the internal nodes are found by iterating (1) with the boundary condition (3).

In the discrete case, the dynamic mesh can be assembled by adding to every node an artificial mass and to every edge an artificial dashpot and an artificial spring to get the damping and the stiffness matrices, respectively.

Very often in applications, the system (1) is reduced to its quasi-static version resulting in a simplified form

$$\mathbf{K}\mathbf{q} = 0. \tag{4}$$

Numerical solution: Systems of linear equations in the form $K\mathbf{q} = \mathbf{f}$ [such as (4)] are frequently solved with the Jacobi method. This method is an iterative algorithm, where the matrix K is split into two matrices, diagonal matrix K_d and the residual matrix K_r, so that $K = K_d + K_r$, under the assumption of dominant diagonal elements. Hence,

$$K\mathbf{q} = K_d\mathbf{q} + K_r\mathbf{q}. \tag{5}$$

This implies

$$K_d\mathbf{q} = K\mathbf{q} - K_r\mathbf{q} = \mathbf{f} - K_r\mathbf{q}. \tag{6}$$

Finally, we can derive an expression for $\mathbf{q}$ which can serve as a base for iterative solutions $\mathbf{q}^{(k+1)}$:

$$\mathbf{q} = K_d^{-1}(\mathbf{f} - K_r\mathbf{q}) \implies \mathbf{q}^{(k+1)} = K_d^{-1}(\mathbf{f} - K_r\mathbf{q}^{(k)}); \tag{7}$$

where $k+1$ is the number of the iteration. The algorithm is iterated until it converges, i.e., $\mathbf{q}^{(k+1)}$ is equal or close enough to the desired solution. Alternatively to the system approach, the solution can also be found on the element-to-element basis, which takes the following form for an element i:

$$q_i^{(k+1)} = \frac{1}{k_{ii}}\left(f_i - \sum_{j\neq i} k_{ij}q_j^{(k)}\right), \quad i = 1, 2, \ldots, n. \tag{8}$$

We will be employing the Jacobi method in the sequel for solving the system of stent forces.

2) Lineal Springs: The idea behind the spring analogy methods entails replacing the mesh by fictitious springs, as schematically depicted in Fig. 3(b). Each spring then behaves according to Hooke's law, which can be written for the force $\boldsymbol{F}_i$ acting on node i from its neighbors as follows:

$$\boldsymbol{F}_i = \sum_{j=1}^{n_i} k_{ij}(\boldsymbol{\delta}_j - \boldsymbol{\delta}_i), \tag{9}$$

with $\boldsymbol{\delta}_i$ indicating the displacement of the vertex i and n_i—the number of vertices directly connected to i, k_{ij} stands for the stiffness of the spring connecting the vertices i and j [33].

Assuming that in equilibrium the force acting on each node is zero, the nodal displacement can be calculated at every time step as a weighted average of the displacements of the neighboring vertices. This gives the following iterative equation (10), which can be derived from (9) by setting the force to zero (k is the number of iterations):

$$\boldsymbol{\delta}_i^{(k+1)} = \frac{\sum_{j=1}^{v_i} k_{ij}\boldsymbol{\delta}_j^{(k)}}{\sum_{j=1}^{v_i} k_{ij}}. \tag{10}$$

In the case of a moving boundary problem, the known displacements are prescribed to the boundary nodes and then the iterative equation (10) is solved for displacements for all internal nodes on the vertex-to-vertex basis. After a sufficient number of iterations, the new nodal coordinates are determined by adding the final displacement to the old coordinates.

The value of the springs stiffness has implications on how the boundary deformation is propagated to the inner parts of the mesh. Usually the stiffness of lineal springs is set to be inversely proportional to the segment length before the deformation [28]. The intuition behind such a stiffness setting is that mesh vertices that are located in close proximity to each other should exert a stronger restoring force onto each other.

Application to stent expansion: We have developed a method that draws inspiration from the springs analogy and determines mesh movements *without* known boundary deformations. Since crimping of the stent creates spring forces acting inside the structure, the idea is to allow the nodes in the mesh to move under these forces. The movement takes into account the nodal intertwinement with its neighbors by means of the nodal stiffness, the value of which is set to be equal to the sum of all the springs' stiffness connecting it to the direct neighbors. The point to note is that the background mesh of the SG device is also viewed as consisting of springs which are contributing to the expansion process.

In the expansion procedure, we need to distinguish between the two different displacements (deltas). The first one is responsible for the current configuration of the stent, that is, it accounts for the remaining crimping status of the structure. This delta, that we call *crimping delta* δ^{cr}, is used to calculate restoring forces in the current (partially) crimped stent. The second delta, called *expansion delta* δ^{exp}, is the actual displacement with which the stent in expanding in each iterative step. It is used to update the

Incremental Displacement Algorithm for Free Expansion:

1) **Calculate initial displacement of stent vertices** by subtracting the load-free coordinates from the current crimped coordinates. For a vertex i:

$$\boldsymbol{\delta}_i^{cr} = \begin{pmatrix} \delta_{x_i}^{cr} \\ \delta_{y_i}^{cr} \\ \delta_{z_i}^{cr} \end{pmatrix} = \begin{pmatrix} x_i^{cr} \\ y_i^{cr} \\ z_i^{cr} \end{pmatrix} - \begin{pmatrix} x_i^{lf} \\ y_i^{lf} \\ z_i^{lf} \end{pmatrix}$$

2) **Iterate** until there is almost no change in expansion delta $\boldsymbol{\delta}^{exp}$: stop when $max\{|\delta_{x_i}^{exp}|, |\delta_{y_i}^{exp}|, |\delta_{z_i}^{exp}|\} \leq \epsilon\ (= 10^{-6})$ for all internal nodes
   a) **Calculate restoring force** $\boldsymbol{F}_i$ for each node i

$$\boldsymbol{F}_i = \sum_{j=1}^{n_i} k_{ij}(\boldsymbol{\delta}_j^{cr} - \boldsymbol{\delta}_i^{cr})$$

   b) **Calculate expansion delta** $\boldsymbol{\delta}_i^{exp}$ for each node

$$\boldsymbol{\delta}_i^{exp} = -\frac{\boldsymbol{F}_i}{\sum_{j=1}^{v_i} k_{ij}} \tag{11}$$

   c) **Update stent** nodal coordinates for each node i by adding the expansion delta

$$\begin{pmatrix} x_i^{cr} \\ y_i^{cr} \\ z_i^{cr} \end{pmatrix} := \begin{pmatrix} x_i^{cr} \\ y_i^{cr} \\ z_i^{cr} \end{pmatrix} + \begin{pmatrix} \delta_{x_i}^{exp} \\ \delta_{y_i}^{exp} \\ \delta_{z_i}^{exp} \end{pmatrix}$$

   d) **Update crimping delta** values $\boldsymbol{\delta}_i^{cr}$ for each i by adding $\boldsymbol{\delta}_i^{exp}$ to the previous $\boldsymbol{\delta}_i^{cr}$

$$\boldsymbol{\delta}_i^{cr} = \begin{pmatrix} \delta_{x_i}^{cr} \\ \delta_{y_i}^{cr} \\ \delta_{z_i}^{cr} \end{pmatrix} := \begin{pmatrix} \delta_{x_i}^{cr} \\ \delta_{y_i}^{cr} \\ \delta_{z_i}^{cr} \end{pmatrix} + \begin{pmatrix} \delta_{x_i}^{exp} \\ \delta_{y_i}^{exp} \\ \delta_{z_i}^{exp} \end{pmatrix}$$

3) **Determine coordinates** of the stent in the global coordinates from newly found local coordinates.

stent vertices' coordinates in the process of deployment. During the deployment process, the two deltas feed into each other.

First, the initial δ^{cr} is determined, which measures the initial crimping deformation. The iterative process starts with the calculation of the restoring forces inside the mesh based on the crimping delta δ^{cr}. Based on this information and stiffness of the vertices, each iterative step of the expansion process determines the current displacement δ^{exp}. Afterward, the current coordinates of stent vertices are updated, as well as δ^{cr}, so that they both correspond to the current status of crimping in the stent structure. The process is repeated until there is no change in the stent structure, that is, no restoring forces are acting on the struts (see the detailed pseudocode of the Incremental Displacement Algorithm for Free Expansion in the box above).

3) Semitorsional Springs: The driving force of the lineal spring analogy is the restoring force created by the stiffness of an edge. However, the process of stent expansion is mostly governed by angular displacements of the stent struts and angular forces. Hence, we investigate an extension of the lineal spring analogy called "semitorsional spring analogy" that takes the angular information into account. The idea is to provide additional stiffening elements by placing a torsional spring at each node of the mesh. The torsion spring would account for the angular displacement of mesh elements and enable controlling mesh deformation. Based on the lineal spring analogy, the behavior of the torsion spring is modeled indirectly by integrating the element's angular values into the stiffness of the spring edge, giving rise to the *semitorsional* stiffness. Fig. 3(c) schematically demonstrates the idea behind the approach for a 2-D mesh showing torsional springs placed at the corners between adjacent edges of a triangular element.

There have been different proposals in the literature as to how to define the semitorsional stiffness. We have used the definition suggested by [34] that calculates the semitorsional stiffness of an edge ($k_{ij}^{\mathrm{semitorsional}}$) by gathering angular information from all facing edges in a sum

$$k_{ij}^{\mathrm{semitorsional}} = \kappa \sum_{m=1}^{n_{ij}} \frac{1}{\sin^2 \theta_m^{ij}}; \tag{12}$$

where n_{ij} is the number of all triangular elements that includes the edge $(i-j)$, θ_m^{ij} is the angle facing the edge $(i-j)$ in one of such triangular elements (m), and κ is a parameter for controlling the dimensionality of the resulting stiffness.

Since the value of the sine approaches 0 when the angle approaches 0 or π, the facing edge becomes very stiff when neighboring edges are close to collision. Stiffening the edge slows down the progression in the angle change, preventing thereby the unwanted inversion of elements. Then, the total stiffness of an edge is composed of the sum of the two types of stiffness, the lineal and the semitorsional

$$k_{ij} = k_{ij}^{\mathrm{lineal}} + k_{ij}^{\mathrm{semitorsional}}. \tag{13}$$

The procedure for free expansion is the same as in the lineal case that has been reported in Section II-B2.

4) Torsional Springs: Another proposal to control the angular deformations of the mesh elements has been to directly implement the artificial torsional springs added to the nodes of the mesh (and not to merely simulate them, as in the previous approach). Then, the torsional stiffness of a torsional spring attached to a vertex i can be defined as

$$C_i^{ijk} = \frac{1}{1+\cos\theta_i^{ijk}} \times \frac{1}{1-\cos\theta_i^{ijk}} = \frac{1}{\sin^2\theta_i^{ijk}}; \tag{14}$$

where C_i^{ijk} is the stiffness of the spring that is attached to the vertex i which is connected with vertices j and k and, thus, associated with the angle θ_i^{ijk} (see Fig. 4), as proposed by Farhat *et al.* [32]. Hence, this torsional spring will create torques opposing the change in the angle. We will show the derivation of the torsional method for the 2-D case and then extend it to the 3-D version which is employed for the stent expansion simulation.

a) Kinematics: We use the kinematic formulation proposed by Farhat *et al.* [32] that was developed under the assumption that only small displacements and rotations occur between two subsequent time steps. The assumption is necessary during the derivation in order to get angular displacements to

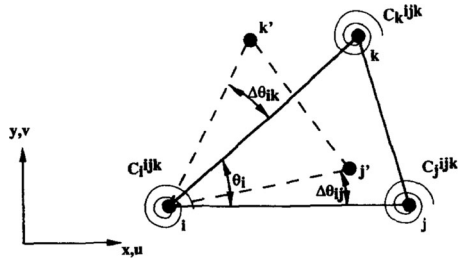

Fig. 4. Schematic representation of the torsional spring analogy: an artificial torsional spring is placed at each node controlling angular deformation [32].

be expressed in terms of vertices displacements in a linear way. Thus, the iterative algorithm based on this method has to sufficiently break down the large deformation that might occur in the course of the simulation into small ones in order to respect the assumption.

Coming back to Fig. 4, we consider the displacement of a 2-D triangle Δ^{ijk} from its reference position, depicted by a solid line, into a current configuration, shown by a dashed line in the image. The displacement components resulting from the displacement of the triangle vertices i, j, and k are captured in the vector $\boldsymbol{q}$ defined in the following way:

$$\boldsymbol{q}^{ijk} = [\, u_i \quad v_i \quad u_j \quad v_j \quad u_k \quad v_k \,]'.$$

The resulting rotation increment is denoted by the vector

$$\boldsymbol{\Delta}\theta^{ijk} = [\, \Delta\theta_i \quad \Delta\theta_j \quad \Delta\theta_k \,]'.$$

The rotation increment $\boldsymbol{\Delta}\theta^{ijk}$ can be defined in the matrix form in the following way:

$$\boldsymbol{\Delta}\theta^{ijk} = \boldsymbol{R}^{ijk}\boldsymbol{q}^{ijk}, \tag{15}$$

where the matrix $\boldsymbol{R}^{ijk}$ is composed as follows: $\boldsymbol{R}^{ijk} =$

$$\begin{bmatrix} b_{ik}-b_{ij} & a_{ij}-a_{ik} & b_{ij} & -a_{ij} & -b_{ik} & a_{ik} \\ -b_{ji} & a_{ji} & b_{ji}-b_{jk} & a_{jk}-a_{ji} & b_{jk} & -a_{jk} \\ b_{ki} & -a_{ki} & -b_{kj} & a_{kj} & b_{kj}-b_{ki} & a_{ki}-a_{kj} \end{bmatrix} \tag{16}$$

and the components of the $\boldsymbol{R}^{ijk}$ matrix are built as

$$a_{ij} = \frac{x_{ij}}{l_{ij}^2}, \quad b_{ij} = \frac{y_{ij}}{l_{ij}^2} \quad \forall(i,j).$$

b) Equilibrium: In order to express the moments produced by torsional springs as forces acting on the mesh, we first write these moments in a matrix form according to the angular version of Hooke's law

$$\boldsymbol{M}^{ijk} = \boldsymbol{C}^{ijk}\boldsymbol{\Delta}\theta^{ijk},$$

where

$$\boldsymbol{M}^{ijk} = \begin{bmatrix} \boldsymbol{M}_i \\ \boldsymbol{M}_j \\ \boldsymbol{M}_k \end{bmatrix}; \quad \boldsymbol{C}^{ijk} = \begin{bmatrix} \boldsymbol{C}_i^{ijk} & 0 & 0 \\ 0 & \boldsymbol{C}_j^{ijk} & 0 \\ 0 & 0 & \boldsymbol{C}_k^{ijk} \end{bmatrix}.$$

Substituting the expression for $\boldsymbol{\Delta}\theta^{ijk}$ defined in (15), we get

$$\boldsymbol{M}^{ijk} = [\boldsymbol{C}^{ijk}\boldsymbol{R}^{ijk}]\boldsymbol{q}^{ijk}.$$

In order to attach the additional torsional springs to a lineal spring mesh, Farhat *et al.* [32] have proposed the transformation of the moments $\boldsymbol{M}^{ijk}$ into a set of equivalent forces at each vertex gathered in vector $\boldsymbol{F}^{ijk}_{\text{torsion}}$ as

$$\boldsymbol{F}^{ijk}_{\text{torsion}} = [\, F_{i_x} \quad F_{i_y} \quad F_{j_x} \quad F_{j_y} \quad F_{k_x} \quad F_{k_y} \,]'_{\text{torsion}}.$$

$\boldsymbol{F}^{ijk}_{\text{torsion}}$ can be deduced from moments $\boldsymbol{M}^{ijk}$ by a linear transformation with the help of the matrix $\boldsymbol{R}^{ijk^T}$ as follows (the detailed derivation is reported in [32]):

$$\boldsymbol{F}^{ijk}_{\text{torsion}} = \boldsymbol{R}^{ijk^T}\boldsymbol{M}^{ijk}.$$

Finally, Farhat *et al.* [32] define for every element $\boldsymbol{\Delta}^{ijk}$ the equivalent forces $\boldsymbol{F}^{ijk}_{\text{torsion}}$ produced by the torsional springs as

$$\boldsymbol{F}^{ijk}_{\text{torsion}} = [\boldsymbol{R}^{ijk^T}\boldsymbol{C}^{ijk}\boldsymbol{R}^{ijk}]\boldsymbol{q}^{ijk} = \boldsymbol{K}^{ijk}_{\text{torsion}}\boldsymbol{q}^{ijk}. \tag{17}$$

c) Dimensionality issues: In order to properly integrate both types of springs, some modifications to the original definition of torsional forces proposed by Farhat *et al.* [32] had to be made. The reason for the alteration is the discrepancy in dimensionality in both types of forces [36]. More precisely, the lineal spring forces are nondimensional quantities, since lineal stiffnesses k_{ij} is inversely proportional to segment lengths (9). In contrast to that, the torsional forces are dimensional quantities. This is because the torsional stiffness is defined in (17), where $\boldsymbol{C}^{ijk}$ is dimensionless and $\boldsymbol{R}^{ijk}$ is inversely proportional to the length (16). Hence, $\boldsymbol{K}^{ijk}_{\text{torsion}}$ is inversely proportional to length square, resulting in torsional forces being inversely proportional to the length. Therefore, if we simply added the torsional spring forces to the lineal spring forces, the relative importance of the lineal and torsional springs would depend on the choice of the length units (for example, either meters or millimeters), which clearly should not be the case. In order to avoid this undesirable effect, we have redefined torsional spring forces as nondimensional quantities by scaling the torsional stiffness according to a characteristic length

$$\boldsymbol{C}^{ijk} = \frac{\kappa}{\sin^2\theta_i^{ijk}} \tag{18}$$

where scaling constant $\kappa = \frac{\ell}{c}$ can be defined through the local characteristic length ℓ of the mesh, such as the average edge length of a triangular element, scaled with a chosen constant c. By the way, the same applies to the semitorsional method and the overlay between the lineal and the semitorsional springs. There as well, the parameter κ was used to control the dimension [see (12)].

d) Numerical solution algorithm: We have used the Jacobi scheme to solve the system $\boldsymbol{K}\boldsymbol{\delta} = \boldsymbol{f}$ on a vertex-by-vertex basis, making the following transformation to the original definition given by (7)

$$\begin{aligned} \boldsymbol{\delta}^{(n+1)} &= \boldsymbol{K}_d{}^{-1}(\mathbf{f} - \boldsymbol{K}_r\boldsymbol{\delta}^{(n)}) \\ &= \boldsymbol{K}_d{}^{-1}(\mathbf{f} - (\boldsymbol{K} - \boldsymbol{K}_d)\boldsymbol{\delta}^{(n)}) \\ &= \boldsymbol{K}_d{}^{-1}\mathbf{f} - \boldsymbol{K}_d{}^{-1}\boldsymbol{K}\boldsymbol{\delta}^{(n)} + \boldsymbol{K}_d{}^{-1}\boldsymbol{K}_d\boldsymbol{\delta}^{(n)} \\ &= \boldsymbol{K}_d{}^{-1}\mathbf{f} - \boldsymbol{K}_d{}^{-1}\boldsymbol{K}\boldsymbol{\delta}^{(n)} + \boldsymbol{\delta}^{(n)}. \end{aligned}$$

Noting that the system should approach static equilibrium, that is, $\boldsymbol{f} = \boldsymbol{0}$, and substituting in the above expression $\boldsymbol{K}\boldsymbol{\delta}^{(n)} = \boldsymbol{F}^{(n)}$, the final iterative algorithm for the torsional springs model can be summarized in the form as follows:

$$\begin{aligned} \boldsymbol{F}^{(n)} &= \boldsymbol{K}_{\text{lineal}}\boldsymbol{\delta}^{(n)} + \boldsymbol{K}_{\text{torsion}}\boldsymbol{\delta}^{(n)} \\ \overline{\boldsymbol{\delta}^{(n+1)}} &= \boldsymbol{\delta}^{(n)} - (\boldsymbol{K}_{\boldsymbol{d}\,\text{torsion}} + \boldsymbol{K}_{\text{lineal-nodal}})^{-1}\boldsymbol{F}^{(n)} \\ \boldsymbol{\delta}^{(n+1)} &= \omega\,\overline{\boldsymbol{\delta}^{(n+1)}} + (1-\omega)\,\boldsymbol{\delta}^{(n)}. \end{aligned} \tag{19}$$

Note that in every iteration, torsional and lineal spring forces are computed separately and added afterward to obtain the total force $\boldsymbol{F}^{(n)} = \boldsymbol{K}_{\text{lineal}}\boldsymbol{\delta}^{(n)} + \boldsymbol{K}_{\text{torsion}}\boldsymbol{\delta}^{(n)}$ due to different structural organization of stiffness matrices $\boldsymbol{K}_{\text{lineal}}$ and $\boldsymbol{K}_{\text{torsion}}$. Since the Jacobi method is operating on the inverse diagonal matrix in every iteration (see Section II-B1), the diagonal components of both stiffness matrices have to be incorporated to overlay the effect of lineal and torsional springs, which is equivalent to adding the two matrices $\boldsymbol{K}_{\boldsymbol{d}\,\text{torsion}} + \boldsymbol{K}_{\text{lineal-nodal}}$. The relaxation parameter ω was permanently set to 0.5.

e) Extension to 3-D stent case: The main idea for the modification is to use the 2-D torsional spring analogy in the plane of each triangular element and then transfer the results to the 3-D stent world. More precisely, since the stent struts are modeled without taking the thickness into account, each of the triangular elements lies in a 2-D plane, defined by its three points. Thus, it is possible to perform computations in the local coordinate system of the triangular elements, applying the 2-D torsional method and then convert the obtained forces, displacements, etc., to the global coordinate system. Alternatively, we could convert the "local" stiffness matrix obtained for 2-D case into a global 3-D stiffness matrix, which is then used for calculation of forces and displacements in the global coordinate system. We have chosen the latter way, since it does not require storing in memory all the local bases and conversion of displacements into these local coordinate bases.

Hence, after the 2-D stiffness was obtained, we have to transform this stiffness matrix to the global coordinate system. We do that by multiplying it with the basis vectors of the local coordinate system, which is actually a rotation matrix ($\boldsymbol{R}$) and can be used to switch between the two coordinate systems:

$$\boldsymbol{K}^{ijk}_{\text{torsion-global}} = \boldsymbol{R}\,\boldsymbol{K}^{ijk}_{\text{torsion-local}}\,\boldsymbol{R}^{T}. \tag{20}$$

For the stent expansion process, we use the same iterative method that was used in the 2-D case; one iteration is summarized in (19). With respect to the forces' vector, as before, it contains a sum of both types of forces: lineal overlaid with torsional. This iteration substitutes the Step 2 (Iterate) in the incremental displacement algorithm, described in Section II-B2, which models the free expansion procedure.

C. Modeling the Vessel and the Contact

1) Geometry Reconstruction: Clinical imaging data are usually obtained in the DICOM format. A sequence of the DICOM images that capture different "slices" of the scanned part of the body in 2-D can be combined to reproduce a 3-D representations of the scanned organ in the process of *segmentation*. The outcome of the segmentation is a 3-D representation that can be stored as an STL (stereolithography) or any other CAD-like 3-D geometric definition format. For example, the STL file will contain a description of the surface by listing unstructured triangles that make up its mesh, where each triangle is described by the 3-D coordinates of the three vertices that comprise it and the normal to the triangle plane.

2) Contact: The expansion process of the stent is performed on a vertex-by-vertex basis, and the coordinates of a vertex are updated in each iteration as long as no contact between the vertex and the vessel occurs. The check for the contact is performed after Step (b) in the incremental displacement algorithm, where the expansion displacement is calculated for each node and before the nodal update in Step (c). Contact is defined to occur when the distance between the vertex of the stent and any of the vessel's vertices becomes smaller than a chosen parameter ϵ. After contact is detected, the displacements for the vertex in contact are still calculated in future iterations. However, its position can only change if it is located within the ϵ-boundary of the vessel inner surface.

III. Results

We have performed deployment experiments for two different devices in different vessel geometries in order to compare the three methods. The two devices were chosen to represent "typical" devices used in the two distinct areas of radiological procedures of interest—aortic and cerebral cases.

1) The first device is a SG corresponding to the GORE TAG Thoracic Endoprosthesis (model TGT4010) with dimensions of 4 cm in diameter and 10 cm in length [see Fig. 1(b)]. The device has 164 struts that are 13 mm in length (on average) and 0.35-mm thick. It is one of the most widely used devices in radiological procedures to treat thoracic aortic aneurysms and aortic dissections.
2) A FD is similar to the commercially available PED, ev3, Irvine, CA, USA) with the diameter of 3 mm and the length of 14 mm [see Fig. 1(c)], which is one of the two devices currently used in Europe to treat cerebral aneurysms. The device has 3200 struts that are 0.4 mm in length.

The stents were crimped to simulate their positioning in the catheter and aligned along the centerline of the target vessel at the relevant positions using the methods described in previous sections. For the first device, the initial crimping was to 20% of its labeled diameter; since in the clinical practice, the SG is compressed into a 24 FR (1FR = 0.333 mm) catheter system, i.e., from 40-mm-outer diameter to 8 mm ($24 \times 0.333 = 8$ mm). With respect to the second device, the PED is usually delivered via a 3 FR microcatheter ($3 \times 0.333 = 1$ mm); hence, it was crimped to the 33% of its load-free diameter.

In all simulations, dimensionality parameters were set to $\kappa = \frac{3}{\ell}$ for the semitorsional method (12), where ℓ is the characteristic length of the device element, measured as an average length of a strut. For the torsional case, the scaling was with $\kappa = \frac{\ell}{3}$ (18). These settings were found to produce the best and most stable results, which were in good alignment with the results of the full FEA simulation performed in our validation study [36]. We can iterate here in brief that the error reported in that paper for the springs method was between 2% and 10%, depending on

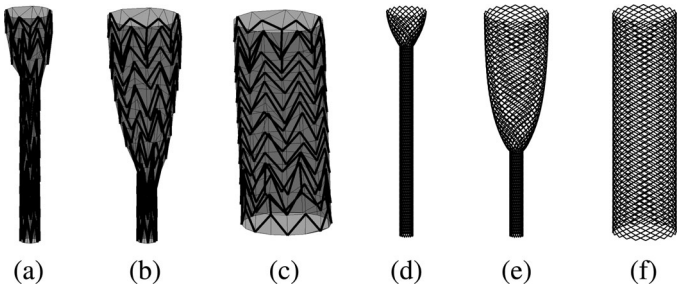

Fig. 5. Free expansion of stents with the lineal spring method: after 10, 100 iterations of layered expansion and at the end of the expansion process, (a)–(c) for the SG and (d)–(f) for the FD, respectively.

the complexity of the case—values that are deemed perfectly acceptable in this context.

To compare the methods and evaluate the results, we define the following metrics of convergence.

1) *Mean nodal distance* between load-free and expanding stent: $\overline{\delta} = \frac{1}{N}\sum_{i=1}^{N} \|n_i - n_i'\|$, where n_i is the position of the node i in the load-free stent and n_i'—in the current expanding stent ($\overline{\delta}$ is measured in millimeters).
2) *Mean angle difference* between load-free and expanding stent: $\overline{\theta} = \frac{1}{M}\sum_{j=1}^{M} |\theta_j - \theta_j'|$, where θ_j is the value of the angle j in the load-free stent, θ_j'—in the current expanding stent, and M stands for the number of angular elements in the stent structure ($\overline{\theta}$ is measured in degrees).
3) *Mean relative strut length difference* between load-free and expanding stent: $\overline{L} = \frac{1}{S}\sum_{k=1}^{S} \frac{|l_k - l_k'|}{l_k}$, where l_k is the length of the strut k in the load-free stent, l_k'—in the current expanding stent, and S stands for the number of struts ($\overline{L}$ is measured in $\%$ relative to the initial length).
4) *Mean nodal force* in expanding stent: $\overline{F} = \frac{1}{N}\sum_{i=1}^{N} \|\boldsymbol{F}_i\|$, where $\boldsymbol{F}_i$ is the reaction force at the node i with the index i running from 1 to N.

We have conducted experiments in four different deployment scenarios, reported in the coming sections:

a) free expansion;
b) deployment in a straight tube;
c) deployment in a bent tube;
d) deployment in real vessel geometries: dissection case for SG and aneurysm case for FD.

All models were implemented in MATLAB and executed on an Intel Core 2 Duo with CPU 2.66 GHz with 4 GB of memory and without using any parallelization—a modest setup easily reproducible in any clinic.

A. Free Expansion

1) SG: From the initially crimped configuration (8 mm in diameter which is 20% of the labeled diameter), the SG device was subject to free expansion until it reached its load-free configuration. Fig. 6 captures the evolution of the expansion process during 300 iterations. The four different convergence metrics are plotted for each of the three springs methods: lineal springs in blue, semitorsional springs in green, and torsional springs in red. Since the released SG is going to "spring back" to its load-free configuration, the shape of which is also known, the clear way to demonstrate the expansion process is to track the distance to the target load-free stent. Hence, we have measured the average distance from the vertices of the current expanding stent to their counterparts in the load-free device (*mean nodal distance*), which is displayed in the first graph in the upper left corner. All three spring methods are able to reach the load-free configuration; however, they do so with different speed, with the lineal method being the fastest and the torsional method being the slowest (completely converges only after about 500 iterations).

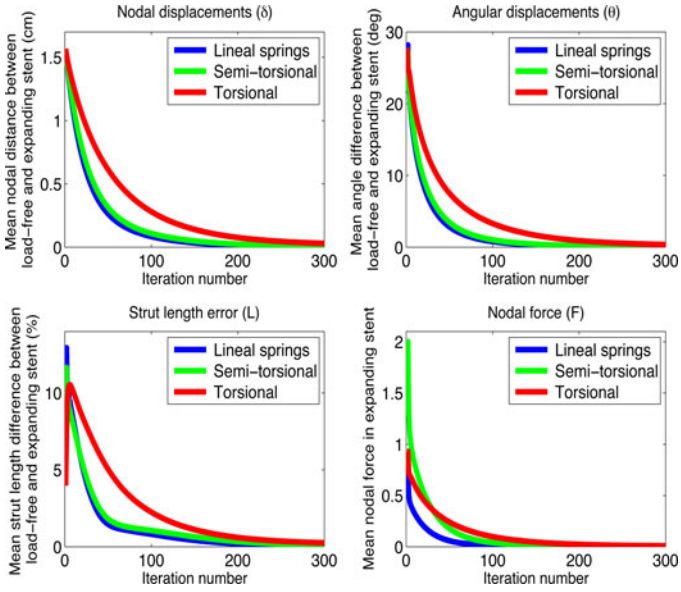

Fig. 6. Free expansion of the SG device for 300 iterations. Upper row: mean nodal distance ($\overline{\boldsymbol{\delta}}$) and mean angle difference ($\overline{\boldsymbol{\theta}}$) between load-free and expanding stent. Bottom row: mean strut length difference ($\overline{\boldsymbol{L}}$) and mean nodal force in the expanding stent ($\overline{\boldsymbol{F}}$). All three methods were able to reach the load-free configuration. The lineal springs method (in blue) displayed the fastest convergence, after 200 iterations. The semitorsional springs method (green) is the second fastest, converging after 250 iterations. The torsional springs method (red) is the slowest, reaching full expansion only after 500 iterations.

The evolution of the angles is shown in the upper right corner as the *mean angle difference* between the load-free and the current expanding stent. This measure is very important since the difference in angles reveals the degree of crimping in the structure and indirectly shows the average angular displacement in every iteration. Again, the lineal method displays faster convergence, semitorsional is similarly fast, and the torsional is the slowest. Equally, it is important to ensure the adequate struts' length evolving throughout the iterative process. This is done by measuring the *mean strut length difference* which gives the average error length as a relative percentage of the initial length. The bottom left graph displays the behavior of struts' length. The initial iterations corrupt the average length up to 14% (for lineal springs method), but it gets corrected in the course of the expansion process.

Finally, the bottom right graph displays the *mean nodal force* in the expanding stent which gives account for the reaction forces guiding the expansion process. The point to note is that the forces for semitorsional and torsional methods include the

TABLE I
VALUES OF CONVERGENCE METRICS AT THE END OF THE DEPLOYMENT PROCESS

Simulation setup	it	$\overline{\delta}$ mm	$\overline{\theta}^{\circ}$	$\overline{\mathrm{L}}\%$	$\overline{\mathrm{F}}$
1) **SG: Free expansion: lin** (3s)	250	0	0	0	0
2) **SG: Free expansion: semi** (4s)	300	0	0	0	0
3) **SG: Free expansion: tors** (40s)	500	0	0	0	0
4) **FD: Free expansion: lin** (26s)	250	0	0	0	0
5) **FD: Free expansion: semi** (31s)	300	0	0	0	0
6) **FD: Free expansion: tors** (120s)	500	0	0	0	0
7) **SG: Straight tube: lin** (24s)	70	$\mathbf{4.2}^{5.1}_{3.6}$	$\mathbf{6}^{19.9}_{0.005}$	$\mathbf{3}^{9.5}_{0.009}$	$\mathbf{0.13}^{0.5}_{0}$
8) **SG: Straight tube: semi**	100	$\mathbf{4.2}^{5.3}_{3.5}$	$\mathbf{6}^{21.9}_{0.002}$	$\mathbf{3}^{10.4}_{0.03}$	$\mathbf{0.29}^{1.9}_{0}$
9) **SG: Straight tube: tors**	170	$\mathbf{3.9}^{6.5}_{3.3}$	$\mathbf{7}^{18.2}_{0.007}$	$\mathbf{3}^{11}_{0.02}$	$\mathbf{0.15}^{1.8}_{0}$
10) **FD: Straight tube: lin** (91s)	45	$\mathbf{0.47}^{0.49}_{0.35}$	$\mathbf{16}^{19}_{13}$	$\mathbf{18.1}^{20}_{15}$	$\mathbf{0.17}^{1.0}_{0}$
11) **FD: Straight tube: semi**	50	$\mathbf{0.47}^{0.5}_{0.36}$	$\mathbf{16}^{18}_{13}$	$\mathbf{18.1}^{21}_{15}$	$\mathbf{0.39}^{2.3}_{0}$
12) **FD: Straight tube: tors**	100	$\mathbf{0.46}^{0.47}_{0.36}$	$\mathbf{16}^{18}_{13}$	$\mathbf{18}^{21}_{16}$	$\mathbf{0.18}^{0.5}_{0}$
13) **SG: Bent tube: lin layers**	120	$\mathbf{5.9}^{12.7}_{1.4}$	$\mathbf{7}^{30}_{0.006}$	$\mathbf{5}^{14.2}_{0.05}$	$\mathbf{0.2}^{2.4}_{0}$
14) **SG: Bent tube: semi** (65s)	150	$\mathbf{5.8}^{12.6}_{1.4}$	$\mathbf{6.5}^{28.5}_{0.008}$	$\mathbf{4.5}^{14.7}_{0.02}$	$\mathbf{0.23}^{3.9}_{0}$
15) **SG: Bent tube: tors**	150	$\mathbf{5.7}^{12.5}_{2.8}$	$\mathbf{6.5}^{29.6}_{0.004}$	$\mathbf{5}^{20.3}_{04}$	$\mathbf{0.4}^{1.3}_{0}$
16) **FD: Bent tube: lin** (91s)	70	$\mathbf{0.59}^{2.6}_{0.01}$	$\mathbf{7}^{20}_{0.3}$	$\mathbf{15}^{31}_{3}$	$\mathbf{0.13}^{0.9}_{0.1}$
17) **FD: Bent tube: semi layers**	370	$\mathbf{0.59}^{2.6}_{0.01}$	$\mathbf{7}^{25}_{0.3}$	$\mathbf{15}^{29}_{4}$	$\mathbf{0.3}^{2.7}_{0.4}$
18) **FD: Bent tube: tors**	140	$\mathbf{0.59}^{2.8}_{0.01}$	$\mathbf{7}^{27}_{0.03}$	$\mathbf{15}^{30}_{4}$	$\mathbf{0.13}^{0.8}_{0.1}$
19) **SG: Aorta: lin** (12s)	50	$\mathbf{7.4}^{22.1}_{4.8}$	$\mathbf{11.3}^{50.3}_{0.02}$	$\mathbf{5.8}^{25.1}_{0.7}$	$\mathbf{0.3}^{2.6}_{0}$
20) **SG: Aorta: semi layers**	90	$\mathbf{7.4}^{22.5}_{5.1}$	$\mathbf{11.4}^{45.7}_{0.02}$	$\mathbf{5.9}^{25.1}_{0.3}$	$\mathbf{0.7}^{5.3}_{0}$
21) **SG: Aorta: tors** (24s)	80	$\mathbf{7.5}^{23.4}_{5.2}$	$\mathbf{12}^{46.6}_{0.03}$	$\mathbf{5.9}^{25.3}_{0.6}$	$\mathbf{0.3}^{3.9}_{0}$
22) **FD: ICA: lin** (126s)	200	$\mathbf{0.5}^{2.8}_{0.1}$	$\mathbf{4.5}^{47}_{0.02}$	$\mathbf{4}^{27}_{0.01}$	$\mathbf{0.1}^{2.6}_{0}$
23) **FD: ICA: semi**	300	$\mathbf{0.4}^{2.8}_{0.1}$	$\mathbf{4.5}^{46}_{0.01}$	$\mathbf{4}^{26}_{0.01}$	$\mathbf{0.15}^{4.1}_{0}$
24) **FD: ICA: tors layers**	500	$\mathbf{1}^{2.9}_{0.3}$	$\mathbf{4}^{43}_{0.01}$	$\mathbf{10}^{30}_{0.01}$	$\mathbf{0.2}^{3.1}_{0}$

Columns correspond to: **it** – number of iterations required for convergence, $\overline{\boldsymbol{\delta}}$ – mean nodal distance, $\overline{\boldsymbol{\theta}}$ – mean angle difference, $\overline{L}$ – mean strut length difference, $\overline{F}$ – mean nodal force. Min and max values are also shown; they are located on top of each other and next to the mean value highlighted in bold, as in the following notation: mean $^{max}_{min}$.

lineal component, for this is how it is calculated in the algorithms. Consequently, it is to expect that the lineal reaction forces are smaller in magnitude. On the other hand, the semitorsional forces are much larger, even after the lineal component has been subtracted from them (almost three times the lineal value).

2) FD: The FD device was initially crimped to 33% of its labeled diameter and then underwent the free expansion test for 500 iterations. As it was the case for the SG, the lineal springs method displayed the fastest convergence, after about 250 iterations, closely followed by the semitorsional springs. Again, the torsional method converged only after about 500 iterations. The overall behavior of the convergence metrics is similar to the SG case, depicted in Fig. 6. However, there are some differences with respect to the end values, which are recorded in Table I (cases 4–6). All convergence metrics display zero residual value since the FD returned to the load-free configuration. The lineal method was again the quickest, requiring 250 iterations (it) and 26 s (time in brackets).

Fig. 5 illustrates the snapshots of the free expansion for two stents with the lineal spring analogy expansion method.

B. Ideal Vessel: Straight Tube

1) SG: In this set of experiments, the device was deployed inside an idealized vessel in the shape of a straight cylinder. The diameter of the cylinder was 34 mm, which is a usual vessel size for a 40-mm device, because the grafts are always oversized in the clinical practice for about 30%. As before, the device was crimped to 8 mm and deployed, this time until it reached the vessel walls. The snapshots of the expansion with the semitorsional method after a certain amount of iterations are captured in Fig. 7(a)–(c). The other two methods displayed a comparable progression.

Table I (cases 7–9) shows the convergence of parameters throughout the deployment process. The values in the table are displayed in the format $\mathbf{mean}^{\max}_{\min}$, with the average value in bold. The lineal springs method displays the fastest convergence rate again. However, torsional springs perform slightly better this time with respect to the final nodal displacement (see $\overline{\delta}$), which is surprising given their earlier performance in the free expansion case. When the deployment is complete, after about 100 iterations on average, there is a very small but nonzero restoring force that remains due to oversizing, which would help keeping the device placement intact.

2) FD: The PED was crimped to 1 mm and released into an idealized cylinder with the 2.3-mm diameter in order to account for the oversizing. The snapshots of the expansion with the torsional method after a certain amount of iterations are captured in Fig. 7(g)–(i). The other two methods displayed a comparable progression with a slightly faster convergence. The convergence results can be seen in Table I (cases 10–12). The struts length difference remains substantial since struts are not fixed due to the woven design of the device; therefore, the struts can slide, emulated by the flexible nature of the springs.

C. Ideal Vessel: Bent Tube

1) SG: This time the geometry of the vessel was represented as a bent cylinder with a diameter of 34 mm. The lineal springs method was applied in layers, starting from the center of the device, as performed in the clinical practice. Fig. 7(d)–(f) displays the snapshots of the layered lineal expansion after a certain amount of iterations.

Since the lineal springs method was applied in layers, its convergence is slower than its semitorsional and torsional counterparts (see Table I, cases 13–15). The latter two methods displayed a progression comparable to the previous cases, although the semitorsional method is slightly more accurate with respect to the struts' length error. After the deployment is complete, there is a small nonzero restoring force that remains present due to the oversizing of the device and the geometry of the vessel.

Note that metrics that we have used to evaluate the performance of the methods are not suitable for the bent (and more complicated) geometries. For example, the nodal displacements are calculated as the distance from the current expanding stent to the load-free configuration and does not represent a meaningful value, since the load-free configuration is not the target of the expansion this time. In fact, the target is unknown! Nevertheless, we chose to continue to use these familiar metrics merely to compare the difference in the convergence rates of the three methods.

2) FD: The PED was crimped to 1 mm and released in the idealized bent cylinder with the 2.6-mm diameter to account for the oversizing. This time, we have applied the semitorsional method in layers, the snapshots of which can be seen in Fig. 7(j)–(l). The other two methods were applied simultaneously to all

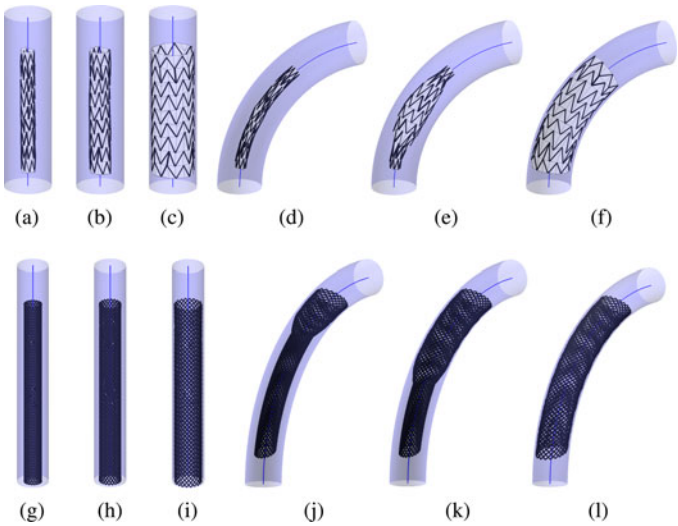

Fig. 7. Expansion of stents in different geometries: (a)–(c) SG expansion from the crimped stent to fully deployed after 100 iterations; (g)–(i) FD expansion from the crimped stent to fully deployed after 100 iterations; (d)–(f) and (j)–(l) layered expansion of the SG and FD devices in bent vessels, respectively.

layers. The general convergence values are depicted in Table I (cases 16–18).

D. Real Vessel Geometries

1) SG: We have tested the performance of the virtual deployment algorithm in the case of the aortic dissection. As it would be done in clinical practice, the graft was placed inside the true lumen to cover the initial tear entry and prevent blood from flowing into the false lumen.

The vessel diameter was varying at the deployment site and ranged between 2.9 and 2.1 cm in the distal and proximal location of the device in the true lumen, respectively. Therefore, we had to adjust the dimensions of the modeled SG to match those that would be required in clinical practice. The modified device featured 3.2-cm diameter and 10-cm length.

The opening of the device was started in the center of the device and was progressing to its extremities, as common with this type of devices. Fig. 8 shows the deployment snapshots at different phases during the deployment process. The final configuration was obtained after approximately 200 iterations of the virtual deployment algorithm and required approximately 30 s. The device was in a good opposition to the vessel wall and has covered the initial tear completely. During the opening of the device, the angles and struts' length progressively approach the values corresponding to the load-free configuration. Table I (cases 19–21) shows the resulting metrics.

2) FD: The final deployment experiment involved a case of a giant aneurysm located in the left ICA artery of a patient (see Fig. 9; note the small opthalmic artery originating on the opposite vessel's wall with respect to the aneurysmal sac). The 3-D vessel geometry featured a variation in vessel's diameter from 4.1 mm in the distal and 4.4 mm in the proximal location with respect to the aneurysm. For such dimensions of the vessel, a FD of 4.5-mm diameter and 14 mm in length could be utilized

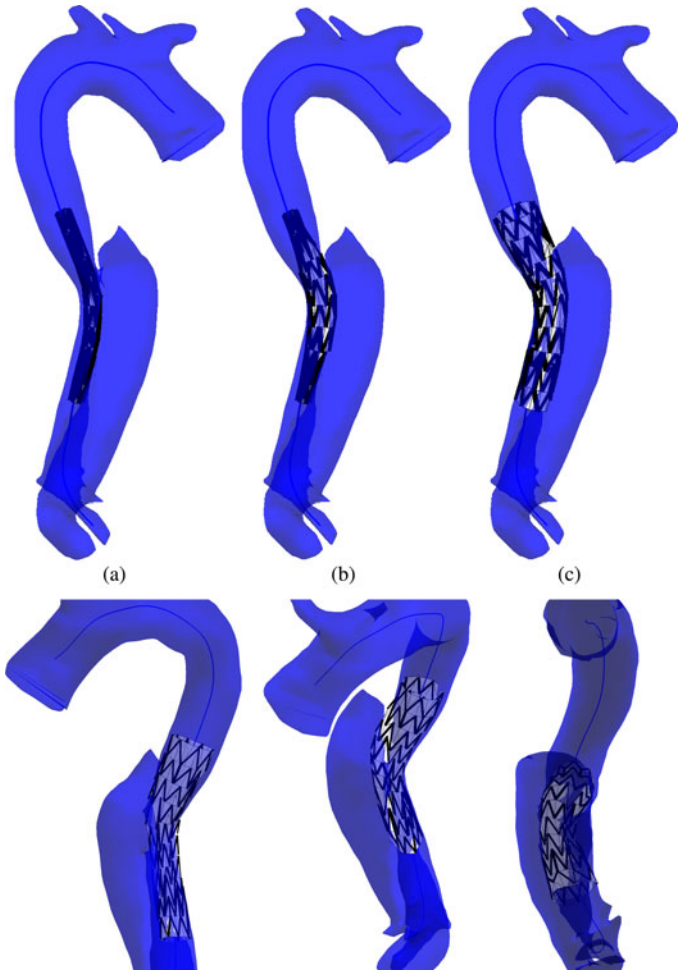

Fig. 8. Virtual SG deployment in the dissected patient's vessel. Upper row: (a) 20%-crimped device initially placed on the centerline of the target vessel on the site of the pathology; (b) and (c) after 50 and 100 iterations of the expansion process, respectively, starting from the central part of the device and propagating to its extremities. Lower row: final configuration of the deployed SG as in (c), displayed from different rotation angles.

in a clinical setting. Therefore, we had to adjust the modeled FD, reconfiguring it to be 4.5 mm in diameter in order to account for both vessel geometry and oversizing. We have deployed the device over the neck of the aneurysm, applying the torsional method in layers.

As it would be the case in real interventions, the opening of the device was started from the distal extremity of the device and progressed to its proximal end, with respect to the aneurysm sac. Fig. 9 shows the deployment snapshots at different phases during the deployment process. The final configuration was obtained after approximately 500 iterations of the virtual deployment algorithm and required about 2.5 min. The device was in a good opposition to the vessel wall. Table I (cases 22–24) shows the resulting metrics.

IV. Conclusion

In this paper, we have reported on methods for virtual stent deployment. The inspiration for the presented algorithms came from the dynamic mesh methods that are widely used in many

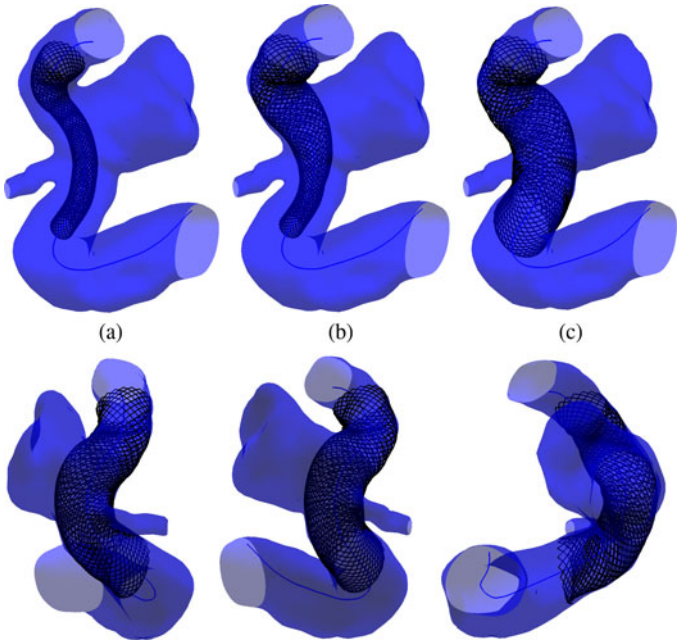

Fig. 9. Virtual FD deployment in a cerebral aneurysmal vessel. Upper row: (a), (b), and (c) after 100, 230, and 500 iterations of the torsional expansion method, respectively, starting from the distal to proximal extremity of the device with respect to the aneurysm sac. Lower row: final configuration of the deployed FD as in (c), displayed from different rotation angles.

engineering applications. Using the spring mesh idea, we have developed algorithms that enable modeling the process of stent expansion and its deployment in vessels. Furthermore, we have compared three different spring analogy methods featuring different properties of the springs and showed their performance in the given problem setting. The three spring analogy methods that were compared are 1) the lineal spring analogy, 2) the semitorsional spring analogy, and 3) the torsional spring analogy. The comparison was based on the results of expansion of two different devices—a SG and a FD—in four different scenarios: 1) in the case of free expansion, 2) in the idealized straight vessels, 3) in the idealized bent vessels, and (4) in real patient cases.

When applied to the stent deployment problem, all three spring analogy methods converged; however, they did so at different rates. The convergence was assessed by different metrics, measuring the displacement and force evolution as well as the evolution of angles between the struts and the struts length. One of the interesting findings entailed the fact that the lineal springs method displays faster convergence rate in all of the four metrics used. Additionally, it produced final results comparable with those obtained by its more sophisticated semitorsional and torsional counterparts. This is surprising since the lineal method constitutes the base for the other two spring methods and is associated with the simplest implementation. In the case of the first device, such outcome for the lineal version was facilitated by the presence of the background mesh, which served as an integrity-preserving element and simulated the angular elements indirectly. For the second device, the fine mesh of the struts effectively produced the effect of the "background" mesh, taking care of the torsional displacements and forces even in the lineal method. In general, the difference in methods is slightly more pronounced for the SG case as compared to the FD (see Table I).

Another characteristic that was similar to all three springs methods was the small residual error in the struts lengths, even in the final stent configuration. This fact is due to the accumulation of imprecisions along the entire deployment processing chain: the crimping, positioning along the centerline, and the sequence of iterations based on the approximative methods. In the future, the methods should pay more attention to this factor with respect to the struts length. It is possible, however, that a special handling of the struts length is necessary for the springs-based methods, for example, incorporation of an additional constraint into the algorithm to preserve or correct the lengths.

With respect to the speed of the virtual simulation, it was sufficiently fast; the longest simulations lasting about 2.5 min for the patient's case of the cerebral aneurysm with the high density PED device on a very modest hardware platform. Gaining a ten times speed up on a state-of-the-art core is certainly within easy reach. Being implemented in MATLAB, so far, with no parallelization and on slow and antiquated hardware, the models are likely to obtain much better speed. Achieving such fast running times is a very positive outcome, for high speed close to real time constitutes one of the top priorities for the development of deployment methods, as outlined in Section I.

Although the lineal spring analogy method proved suitable for modeling the stent expansion, there are still a number of limitations associated with it and this study. The first one to mention is the fact that the validation of the results was omitted here due to space considerations. The detailed validation is reported in another study that is comparing the results reported here with the results of the FEA [36]. The FEA method, although being very slow, can provide validation for the fast springs methods, assess the eventual divergence in the results, and estimate the error. The comparison is, as we discussed, very favorable to the fast method.

The second point worth mentioning is related to the forces. Since the springs methods presented here are approximative, it is not clear what physical meaning is associated with the restoring forces measured by them. From our comparison (see Table I), one can see that the lineal forces feature values that are very similar to those reported by the torsional method; in contrast, the semitorsional method is displaying much higher values. Although from the validation study, we know that the lineal forces lie close to the forces reported by the FEA comparative experiments; the full analysis of the force evolution is yet to be undertaken. In the meantime, one could imagine that although the lineal version is powerful enough to model the movable stent structure [and for now it seems like there is no need for the complex (semi-)torsional springs], the more sophisticated methods could be able to provide better force approximations than the "easy" lineal approach. This would mean that they are actually worthwhile to employ for a more thorough analysis of the deployment process.

Related to the force is the physical meaning of the different types of stiffness and their settings. In this paper, the stiffness

values were assigned in an arbitrary way, disregarding any considerations of the material properties. In the future, the stiffness values have to be reverse engineered in advance in order to account for the mechanical behavior as closely as possible. We hope to gain more understanding of that in *in vitro* experiments with stents, planned for the future. Again, it could turn out that the torsional methods are more suitable for the incorporation of realistic stiffness values than their lineal counterpart.

Other limitations of this study include the treatment of the vessel as a rigid body and the simplified contact model employed. We plan to extend the current model by implementing the stent's self-contact and the possibility of the vessel to deform under the forces exerted by the stent. This would require handling the contact between the two bodies—the interplay of forces and displacements—which would provide valuable information for the clinicians, in order to assess the possible short- and long-term implications of the stent deployment treatment. This further-elaborated model would then be validated against real *in vivo* cases, for which we are gathering pre- and postprocedural data at the moment.

To sum up, this paper demonstrated the overall ability of spring-based methods to model virtual stent expansion in a computationally expedient manner, which constitutes a valuable base for future extensions of the model, with the ultimate goal to enable predictive simulations of the minimally invasive methods in a clinical setting.

ACKNOWLEDGMENT

The authors would like to thank Prof. J. Byrne (University of Oxford) and Dr. H. von Tengg-Kobligk (Inselspital Bern, University of Heidelberg) for their valuable clinical input.

REFERENCES

[1] A. Schanzer and L. Messina, "Two decades of endovascular abdominal aortic aneurysm repair: Enormous progress with serious lessons learned," *J. Amer. Heart Assoc.*, vol. 1, no. 3, pp. e0000752012.

[2] J. Byrne and I. Szikora, "Flow diverters in the management of intracranial aneurysms: A review," *eJ. Eur. Soc. Minimally Invasive Neurolog. Therapy*, vol. 1225000057, 2012.

[3] M. Adriaensen, J. Bosch, E. Halpern, M. Myriam Hunink, and G. Gazelle, "Elective endovascular versus open surgical repair of abdominal aortic aneurysms: Systematic review of short-term results," *Radiology*, vol. 224, no. 3, pp. 739–747, 2002.

[4] A. J. Molyneux, R. S. Kerr, L.-M. Yu, M. Clarke, M. Sneade, J. A. Yarnold, and P. Sandercock, "International subarachnoid aneurysm trial (ISAT) of neurosurgical clipping versus endovascular coiling in 2143 patients with ruptured intracranial aneurysms: A randomised comparison of effects on survival, dependency, seizures, rebleeding, subgroups, and aneurysm occlusion," *Lancet*, vol. 366, no. 9488, pp. 809–817, 2005.

[5] Z. Kulcsar, E. Houdart, A. Bonafe, G. Parker, J. Millar, A. Goddard, S. Renowden, G. Gal, B. Turowski, K. Mitchell, F. Gray, M. Rodriguez, R. van den Berg, A. Gruber, H. Desal, I Wanke, and D. A. Rufenacht, "Intra-aneurysmal thrombosis as a possible cause of delayed aneurysm rupture after flow-diversion treatment," *Amer. J. Neuroradiol.*, vol. 32, no. 1, pp. 20–25, 2011.

[6] P. I. D'Urso, G. Lanzino, H. J. Cloft, and D. F. Kallmes, "Flow diversion for intracranial aneurysms a review," *Stroke*, vol. 42, no. 8, pp. 2363–2368, 2011.

[7] J. Mas, G. Chatellier, B. Beyssen, A. Branchereau, T. Moulin, J. Becquemin, V. Larrue, M. Lièvre, D. Leys, J. Bonneville, J. Watelet, J.-P. Pruvo, J.-F. Albucher, A. Viguier, P. Piquet, P. Garnier, F. Viader, E. Touze, M. Giroud, H. Hosseini, J.-C. Pillet, P. Favrole, J.-P. Neau, and X. Ducrocq, "Endarterectomy versus stenting in patients with symptomatic severe carotid stenosis," *New Engl. J. Med.*, vol. 355, no. 16, pp. 1660–1671, 2006.

[8] D. Fiorella, P. Lylyk, I. Szikora, M. Kelly, F. Albuquerque, C. McDougall, and P. Nelson, "Curative cerebrovascular reconstruction with the pipeline embolization device: The emergence of definitive endovascular therapy for intracranial aneurysms," *J. NeuroIntervent. Surg.*, vol. 1, no. 1, pp. 56–60, 2009.

[9] D. Kiousis, A. Wulff, and G. Holzapfel, "Experimental studies and numerical analysis of the inflation and interaction of vascular balloon catheter-stent systems," *Ann. Biomed. Eng.*, vol. 37, no. 2, pp. 315–330, 2009.

[10] R. Schwartz and T. Henry, "Pathophysiology of coronary artery restenosis," *Rev. Cardiovasc. Med.*, vol. 3, pp. S4–S9, 2002.

[11] P. Watton, N. Raberger, G. Holzapfel, and Y. Ventikos, "Coupling the hemodynamic environment to the evolution of cerebral aneurysms: Computational framework and numerical examples," *J. Biomech. Eng.*, vol. 131, p. 101003, 2009.

[12] M. Jamous, K. Satoh, S. Matsubara, J. Satomi, N. Nakajima, M. Uno, and S. Nagahiro, "Ischemic basilar artery dissecting aneurysm treated by stenting only," *Neurologia Medico-Chirurgica*, vol. 44, no. 2, pp. 77–81, 2004.

[13] S. Cook, P. Wenaweser, M. Togni, M. Billinger, C. Morger, C. Seiler, R. Vogel, O. Hess, B. Meier, and S. Windecker, "Incomplete stent apposition and very late stent thrombosis after drug-eluting stent implantation," *Circulation*, vol. 115, no. 18, pp. 2426–2434, 2007.

[14] B. Lieber, V. Livescu, L. Hopkins, and A. Wakhloo, "Particle image velocimetry assessment of stent design influence on intra-aneurysmal flow," *Ann. Biomed. Eng.*, vol. 30, no. 6, pp. 768–777, 2002.

[15] M. Hirabayashi, M. Ohta, D. Rüfenacht, and B. Chopard, "A lattice Boltzmann study of blood flow in stented aneurism," *Future Generat. Comput. Syst.*, vol. 20, no. 6, pp. 925–934, 2004.

[16] Y. Ventikos, E. Holland, T. Bowker, P. Watton, N. Kakalis, M. Megahed, F. Zhu, P. Summers, and J. Byrne, "Computational modelling for cerebral aneurysms: Risk evaluation and interventional planning," *Brit. J. Radiol.*, vol. 82, no. Special Issue 1, pp. S62–S71, 2009.

[17] D. Chen, M. Muller-Eschner, D. Kotelis, D. Bockler, Y. Ventikos, and H. von Tengg-Kobligk, "A longitudinal study of Type-B aortic dissection and endovascular repair scenarios: Computational analyses," *Med. Eng. Phys.*, vol. 35, pp. 1321–1330, 2013.

[18] J. Golzarian and D. Valenti, "Endoleakage after endovascular treatment of abdominal aortic aneurysms: Diagnosis, significance and treatment," *Eur. Radiol.*, vol. 16, no. 12, pp. 2849–2857, 2006.

[19] M. Gawenda, G. Jaschke, S. Winter, G. Wassmer, and J. Brunkwall, "Endotension as a result of pressure transmission through the graft following endovascular aneurysm repair—An in vitro study," *Eur. J. Vasc. Endovasc. Surg.*, vol. 26, no. 5, pp. 501–505, 2003.

[20] C. Lally, F. Dolan, and P. Prendergast, "Cardiovascular stent design and vessel stresses: A finite element analysis," *J. Biomech.*, vol. 38, no. 8, pp. 1574–1581, 2005.

[21] D. Ma, G. F. Dargush, S. K. Natarajan, E. I. Levy, A. H. Siddiqui, and H. Meng, "Computer modeling of deployment and mechanical expansion of neurovascular flow diverter in patient-specific intracranial aneurysms," *J. Biomech.*, pp. 2256–2263, 2012.

[22] F. Auricchio, M. Conti, M. De Beule, G. De Santis, and B. Verhegghe, "Carotid artery stenting simulation: From patient-specific images to finite element analysis," *Med. Eng. Phys.*, vol. 33, no. 3, pp. 281–289, 2011.

[23] N. Rebelo, R. Fu, and M. Lawrenchuk, "Study of a nitinol stent deployed into anatomically accurate artery geometry and subjected to realistic service loading," *J. Mater. Eng. Perform.*, vol. 18, no. 5, pp. 655–663, 2009.

[24] L. Flórez Valencia, J. Montagnat, and M. Orkisz, "3d models for vascular lumen segmentation in MRA images and for artery-stenting simulation," *IRBM*, vol. 28, no. 2, pp. 65–71, 2007.

[25] S. Appanaboyina, F. Mut, R. Löhner, C. Putman, and J. Cebral, "Computational fluid dynamics of stented intracranial aneurysms using adaptive embedded unstructured grids," *Int. J. Numer. Methods Fluids*, vol. 57, no. 5, pp. 475–493, 2008.

[26] I. Larrabide, M. Kim, L. Augsburger, M. Villa-Uriol, D. Rüfenacht, and A. Frangi, "Fast virtual deployment of self-expandable stents: Method and in-vitro evaluation for intracranial aneurysmal stenting," *Med. Image Anal.*, vol. 16, no. 3, pp. 721–730, 2010.

[27] J. Montagnat, H. Delingette, and N. Ayache, "A review of deformable surfaces: Topology, geometry and deformation," *Image Vis. Comput.*, vol. 19, no. 14, pp. 1023–1040, 2001.

[28] J. Batina, "Unsteady Euler airfoil solutions using unstructured dynamic meshes," *AIAA J.*, vol. 28, no. 8, pp. 1381–1388, 1990.

[29] G. Wheatley, A. Gurbuz, J. Rodriguez-Lopez, V. Ramaiah, D. Olsen, J. Williams, and E. Diethrich, "Midterm outcome in 158 consecutive gore tag thoracic endoprostheses: Single center experience," *Ann. Thorac. Surg.*, vol. 81, no. 5, pp. 1570–1577, 2006.
[30] L. Pierot, "Flow diverter stents in the treatment of intracranial aneurysms: Where are we?" *J. Neuroradiol.*, vol. 38, pp. 40–46, 2011.
[31] D. Stoeckel, C. Bonsignore, and S. Duda, "A survey of stent designs," *Minimally Invas. Ther. Allied Technol.*, vol. 11, no. 4, pp. 137–147, 2002.
[32] C. Farhat, C. Degand, B. Koobus, and M. Lesoinne, "Torsional springs for two-dimensional dynamic unstructured fluid meshes," *Comput. Methods Appl. Mech. Eng.*, vol. 163, no. 1–4, pp. 231–245, 1998.
[33] F. Blom, "Considerations on the spring analogy," *Int. J. Numer. Methods Fluids*, vol. 32, no. 6, pp. 647–668, 2000.
[34] D. Zeng and C. Ethier, "A semi-torsional spring analogy model for updating unstructured meshes in 3d moving domains," *Finite Elements Anal. Design*, vol. 41, no. 11–12, pp. 1118–1139, 2005.
[35] K. Spranger, C. Capelli, G. Bosi, S. Schievano, and Y. Ventikos, "Comparison and calibration of a real-time virtual stenting algorithm using finite element analysis and genetic algorithms," *Comput. Methods Appl. Mech. Eng. (in review)*, 2014.
[36] C. Bottasso, D. Detomi, and R. Serra, "The ball-vertex method: a new simple spring analogy method for unstructured dynamic meshes," *Comput. Methods Appl. Mech. Eng.*, vol. 194, no. 39, pp. 4244–4264, 2005.

Katerina Spranger holds the Dipl.-Inf. degree in Computer Science from the Humboldt University of Berlin, Germany.

She is currently a postgraduate researcher at the Department of Engineering Science at the University of Oxford, U.K. Her research interests include biomedical engineering, simulations of surgical interventions, and predictive computations for medicine.

Yiannis Ventikos holds the Kennedy Chair at University College London, U.K., where he is also the Head of the Department of Mechanical Engineering. His research interests include transport phenomena, (bio)fluid mechanics, clinical computing, minimally invasive interventional devices design and optimization, and biocomplexity. He has received the M.Eng. in Naval Architecture and Marine Engineering and the Ph.D. in Hydrodynamics and Fluid Mechanics from National Technical University of Athens.